Modelling and Characterization of a Compliant Tethered Microgripper for Microsurgical Applications

Maura Power, Carlo A. Seneci, Alex J. Thompson, Guang-Zhong Yang *Fellow, IEEE*

***Abstract*— The development of microscale surgical tools could pave the way for truly minimally invasive microsurgical procedures. This work demonstrates the application of direct laser writing (DLW) using two-photon polymerization (TPP), a rapid prototyping microfabrication technique, to create a tethered, passively actuated three-dimensional gripper with potential applications in microbiopsy. A microgripper design was devised, modelled and optimized. The gripper was then fabricated and characterized for validation of the theoretical model. The results demonstrate that modelling the behavior of compliant microtools provides a useful approximation for the observed trends and, thus, can be utilized in the design of TPP tools. Future work on the incorporation of viscoelastic material into the model will further improve agreement between the predicted and experimental performance.**

I. Introduction

Microrobots have been recognized as one of the key technologies with the capacity to revolutionize medicine [1]. Microrobots can be categorized into two varieties; non-thethered (or swimming-type) and tethered. The goal of swimming microrobots, a popular focus of research, is to disseminate themselves throughout the body, locate their target anatomy and then perform a task. Their functions may range from drug delivery [2] to microbiopsy [3]. However, there are practical and ethical concerns associated with swimming microrobots that need to be overcome, such as safe retrieval. Furthermore, tethered microrobots can more readily overcome the important issues of power delivery and the transmission of control or sensing signals because the tether (which may be, for example, a metal wire or an optical fibre or a hollow channel) provides a direct means of delivery for electrical current, light, air, liquid etc. Therefore, it is also beneficial to research and develop novel, tethered microrobot technologies.

Microgrippers, for applications such as cell manipulation, have been fabricated for many years using standard microfabrication techniques inherited or adapted from the semiconductor industry [4]. Recently, versatile new microfabrication techniques have become available (such as TPP) and offer exciting opportunities to explore new possibilities for microtools, ranging from mechanical to material design. Compliant mechanisms have long been studied at the macroscale, and are an attractive solution for microrobots. They typically do not require assembly, whilst still incorporating dynamic elements. They are inherently 'soft' due to the need to adapt their shape to the task at hand. TPP has already been demonstrated as a viable method for creating simple compliant mechanisms for micromanipulation [5]. In [6], an under-actuated, compliant gripper with features on the scale of a few millimetres demonstrates how compliancy helps self-distribute grasping forces around an object. This gripper [6] served as the initial inspiration for the microgripper presented in this work.

Maura Power, Carlo A. Seneci, Alex J. Thompson and Guang-Zhong Yang are with the Hamlyn Centre for Robotic Surgery, Imperial College London, SW7 2AZ, London, UK (email:m.power13@imperial.ac.uk)

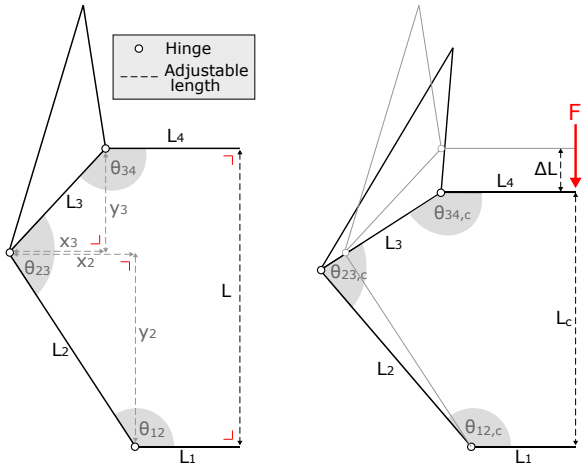

Fig. 1: Gripper finger five-bar closing mechanism

Section 1 describes the microgripper components, Section 2 tackles theoretical modelling, Section 3 discusses the fabrication and characterization process and Section 4 presents a comparison between the theoretical and experimental results.

II. Gripper Overview

The proposed passive gripper incorporates two types of moving elements; flexural hinges and compression springs. The gripper consists of three fingers operating in parallel, and each finger comprises one spring and three hinged joints connected by rigid links.

A. Five-Bar Finger Mechanism

The primary function of the finger is to convert a linear motion - induced by an external force - into a rotational movement of the finger in order to close around a target. This is achieved using a five-bar mechanism, as illustrated in Figure 1. Each finger of the gripper can function fully independently. A spring is incorporated in the design to help to maintain links L_1 and L_4 parallel to each other.

B. Three-Fingered Gripper

For the gripper, three fingers are arranged $120°$ apart to form a fully 3D structure. All three fingers act in parallel

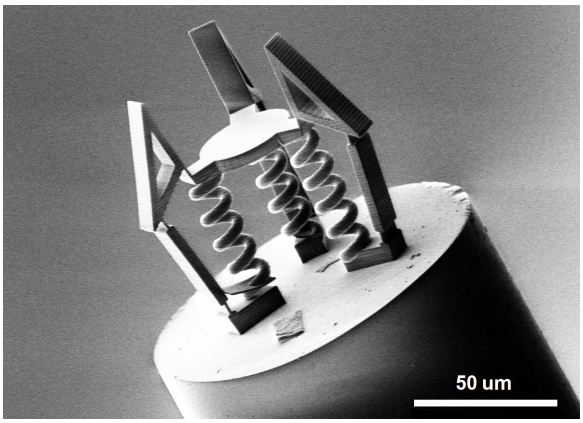

Fig. 2: Gripper printed to tip of optical fibre

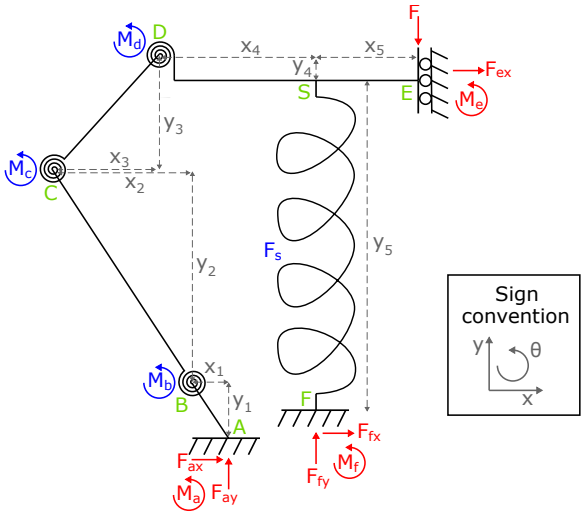

Fig. 3: Static analysis model

and, as a compressive force is applied to the central 'palm' of the gripper, they close inwards. The individual finger design could conceivably, with some modifications to the spring, be fabricated using one of several conventional microfabrication techniques. However, TPP is capable of fabricating arbitrarily complex 3D structures - something that would present a significant challenge using more standard techniques - and, therefore, is uniquely suited to realize such a gripper in a single fabrication step. Figure 2 shows a gripper fabricated to the tip of a 125 μm diameter optical fibre.

Separate springs for each finger - as opposed to a single, central spring - were chosen with future applications in mind, in order to provide integrated sensing capabilities. The sensing features, which we plan to explore in more detail in the future, were not integrated into the design reported in this article as they are outside of the scope of this work and have negligible impact on the mechanical operation of the gripper.

III. Geometric and Static Analysis

This section outlines the mathematical derivations of the generalized geometric and static models of the system; useful for fully understanding and optimizing the gripper design. In addition, there are certain design constraints imposed by both material and fabrication limitations.

The first part of this section relates the relative X- and Y-components of the link lengths to the hinge angles of the fingers (i.e. geometrical measurements only); the second part derives the static analysis model, which accounts for the forces and moments incurred by deformation of the gripper.

A. Geometric Analysis of Five-Bar Mechanism

The geometric analysis describes how the angles between the hinged links of the five-bar mechanism change for a given compression, ΔL. In particular, for this design, the aim is to maximize the change in θ_{34}, which directly affects by how much the gripper fingers close inwards around the object. The generalized model derived in this section is then used in Section V.A to optimize according to this requirement.

Assuming that the lengths of L, L_1, L_2, L_3,and L_4 are known, the angles of the joints can be determined. Due to the construction of the gripper, it can be assumed that L_1 and L_4 translate only in the Y-direction and remain parallel to each other, and that L (the only non-rigid link) describes the Y-axis distance between L_1 and L_4. The original length L changes according to the applied compressive force F resulting in a compressed length of L_c, where

$$L_c = L - \Delta L. \tag{1}$$

The three angles, as marked in Figure 1, that vary as a result of length L being compressed are given by:

$$\theta_{12} = \arcsin\left(\frac{x_2}{L_2}\right) + \frac{\pi}{2} \tag{2}$$

$$\theta_{23} = \arccos\left(\frac{x_2}{L_2}\right) + \arccos\left(\frac{x_3}{L_3}\right) \tag{3}$$

$$\theta_{34} = \arcsin\left(\frac{x_3}{L_3}\right) + \frac{\pi}{2}. \tag{4}$$

The remaining values to be calculated are x_2 and x_3. x_3 is found by solving the quadratic equation

$$\begin{aligned} x_3^2(4L_{41}^2 + 4L_1^2) + x_3(4ZL_{41} + 8L^2L_{41}) \\ +(Z^2 - 4L^2L_2^2 + 4L^2L_{41}^2) = 0 \end{aligned} \tag{5}$$

where Z is defined as

$$Z = L_3^2 - L_2^2 + L_{41}^2 - L^2. \tag{6}$$

L_{41} is already known, and x_2 can be determined by:

$$x_2 = x_3 + L_{41} = x_3 + (L_4 - L_1). \tag{7}$$

B. Static Analysis of Gripper

The static model can be used, in conjunction with the geometrical model, to compute the resultant internal and reaction forces and moments that act on the finger when compressed by ΔL. The full static model is depicted in Figure 3. Joints A and F of the model are fully supported, and Joint E is modelled as a rolling joint that is free to move only in the Y-direction. These behaviors were observed

also during experiments. The hinges at Joints B, C and D are modelled as torsion springs, and the spring as a typical linear spring which is rigidly attached at Joints S and F. The torsion springs and their corresponding moments (M_b, M_c and M_d) are calculated using the torsion spring constant, k_h, and the spring's angular displacement, $\Delta\theta$, according to the following equation:

$$M = k_h.\Delta\theta. \tag{8}$$

Similarly, the linear springs' corresponding forces (F_{sy}) are calculated using their spring constant, k_s, and the linear compression, δ, using Hooke's Law:

$$F = k_s.\delta. \tag{9}$$

The static model is described by 18 equation and has 17 unknowns, making it an overdetermined system. The static model equations are presented below;

1) Full structure:

$$\sum F_{ax} : F_{ay} + F_{fy} - F = 0 \tag{10}$$

$$\sum F_{ay} : F_{ax} + F_{fx} + F_{ex} = 0 \tag{11}$$

$$\begin{aligned} \sum M_a : M_a + M_f + Me \\ +F_{fy}.(x_3 + x_4 - x_1 - x_2) \\ -F_{fx}.(y_1 + y_2 + y_3 - y_4 - y_5) \\ -F.(x_3 + x_4 + x_5 - x_1 - x_2) \\ -F_{ex}.(y_1 + y_2 + y_3 - y_4) = 0 \end{aligned} \tag{12}$$

2) Link 1 (joints A-B):

$$\sum F_{ax} : F_{ax} + F_{bx} = 0 \tag{13}$$

$$\sum F_{ay} : F_{ay} + F_{by} = 0 \tag{14}$$

$$\sum M_a : M_a + M_b - F_{by}.x_1 - F_{bx}.y_1 = 0 \tag{15}$$

3) Link 2 (joints B-C):

$$\sum F_{dx} : -F_{cx} + F_{dx} = 0 \tag{16}$$

$$\sum F_{dy} : -F_{cy} + F_{dy} = 0 \tag{17}$$

$$\sum M_d : -M_b + M_c - F_{cy}.x_2 - F_{cx}.y_2 = 0 \tag{18}$$

4) Link 3 (joints C-D):

$$\sum F_{cx} : -F_{cx} + F_{dx} = 0 \tag{19}$$

$$\sum F_{cy} : -F_{cy} + F_{dy} = 0 \tag{20}$$

$$\sum M_c : -M_c + M_d + F_{dy}.x_3 - F_{dx}.y_3 = 0 \tag{21}$$

5) Link 4 (joints D-E):

$$\sum F_{dx} : -F_{dx} + F_{sx} + F_{ex} = 0 \tag{22}$$

$$\sum F_{dy} : -F_{dy} + F_{sy} = 0 \tag{23}$$

$$\sum M_d : -M_d + M_s + M_e + F_{sy}.x_4 - F.(x_4 + x_5) = 0 \tag{24}$$

6) Spring (joints S-F):

$$\sum F_{fx} : F_{fx} - F_{sx} = 0 \tag{25}$$

$$\sum F_{fy} : F_{fy} - F_{sy} = 0 \tag{26}$$

$$\sum M_f : M_f - M_s + F_{sx}.y_5 = 0 \tag{27}$$

IV. Compliant Mechanism Fabrication and Characterization

This section details the steps involved in fabricating and characterizing the structures in a precise and repeatable manner, seeking to eliminate as much as possible experimental error in order to compare with the theoretical model. Due to the scale of the samples and the unconventional fabrication process, it was necessary to devise a fabrication protocol to control the orientation of the final structure to achieve the most accurate compression and angular displacement measurement under the scanning electron microscope (SEM).

Fixed hinge and spring parameters were chosen to reduce the complexity of this study and to focus on the optimization of the five-bar mechanism. The chosen dimensions are detailed below, and are also used in the final gripper design.

A. Fabrication and Alignment

Cleaved optical fibre was the substrate of choice because it provides a cost-effective, disposable and compatible base (i.e. no adverse affects during laser polymerization). Printing onto an optical fibre is a non-standard application of the DLW system and, therefore, there is no in-built method to align the orientation of the fibre accurately along the printer's X- and Y-axes. As mentioned above, a crucial requirement of the fabrication process is control over the orientation of the tool as it is printed to the fibre. The optical fibre is held vertically using a custom, 3D-printed fibre mount. Once the fibre is held parallel to the DLW system's Z-axis, another custom printed part is used to ensure that the fibre mount is aligned with the system's X- and Y-axes. This process is an improvement upon a similar process detailed in [5]. Another feature of the fibre holder is that the fibre can be accessed from four different directions without moving it from its initial print position, meaning that the structure can be simultaneously compressed by the force sensor and provide a direct line of sight for the SEM.

B. Characterization of Flexural Hinges and Springs

In order to verify the derived static analysis model from Section III, the real linear and torsion spring constants of the hinges and springs, respectively, were first needed. These were found by experimentally obtaining a series of corresponding forces and images of the structure. The changes in the angle of the hinged sections and compression of the springs were determined using template matching during post-processing.

A trend that became apparent in early testing was that the polymer was prone to permanent deformation. This is a well documented phenomena of viscoelastic materials, of which the photoresist [7]. Viscoelastic materials undergo

(a) a) Hinge bent to 0° and 19°

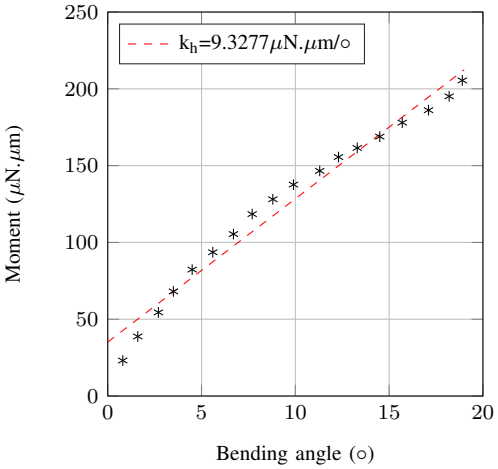

(b) Hinge angle vs. moment results

Fig. 4: Hinge characterization

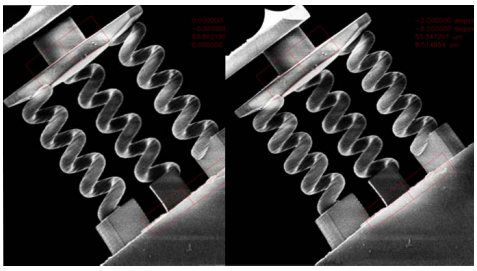

(a) Springs at 0μm and 8μm compression

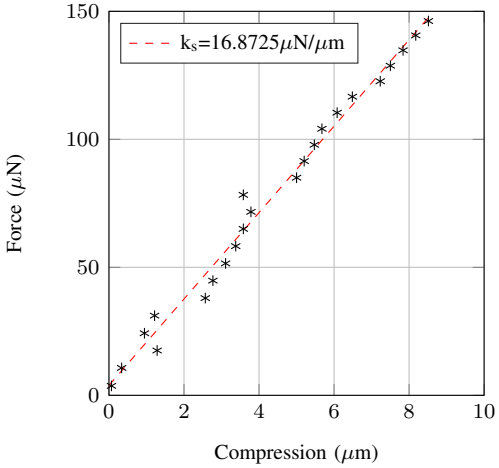

(b) Spring compression vs. force results

Fig. 5: Spring characterization

permanent deformation with increasing stress. Therefore, during the characterization experiments, the structures were not displaced to extremes.

1) Flexural Hinge Characterization: The flexural hinge, as its name suggests, serves as an element in a structure that flexes under torsion in a manner that closely approximates rotation. The hinge is characterized by its torsion spring constant, k_h. The point of rotation is assumed to be the central point of the hinge. The hinge used was 1 μm wide and 4 μm long. When the hinge was not bent, the nominal length of X (the distance from which the force is applied to the centre of the thin hinge section) is L_h = 16.5 μm. As the bending angle increases, the distance X reduces, and k_h can be calculated by:

$$k_h = \frac{M}{\Delta\theta_h} = \frac{F.X}{\Delta\theta_h} = \frac{F.L_h.\sin\Delta\theta_h}{\Delta\theta_h}. \tag{28}$$

A force is applied in discrete, incremental steps until a maximum rotation of 19° is achieved. Previous experiments demonstrated that beyond a certain deflection the deformation of the hinge, once the force was removed, was too great. Figure 4a shows the force sensor bending a hinge, and Figure 4b summarizes the results. The hinge was found to have a torsion spring constant, k_h, of 9.33 μN.m/°.

2) Spring Characterization: The linear spring constant, k_s, is given by:

$$k_s = F/\Delta L. \tag{29}$$

The spring has an initial length of 46.5 μm, a diameter of 14 μm and a circular winding cross-section of 4 μm. Similar to the previous experiment, a certain degree of permanent deformation is observed the more the springs are deformed and so a maximum deformation of 18% of its original length is applied. Again, as with the hinge experiment, a series of incrementally increasing forces were applied to the spring structure, as shown in Figure 5a. Simultaneous force readings and images were acquired, and with the image post-processing the resultant spring constant of the three parallel springs was found to be 16.87 μN/μm, Figure 5b. For parallel springs, the constants are summed, and so the experimentally derived spring constant for a single spring was found to be one third of this value, resulting in k_s equal to 5.62 μN/μm.

V. Final Optimized Design

The goal of this study is to calculate the optimum joint lengths that maximize the gripper closing angle, while also accounting for 1) fabrication and 2) material constraints. First, the printing configuration allows a maximum printing height of 170 μm. In practice, given the manual fibre alignment procedure, this must be reduced in order to ensure the method is easily repeatable allowing for a margin of error. Therefore, a maximum height of 100 μm was chosen.

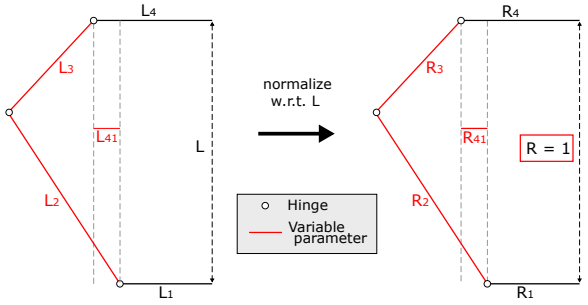

Fig. 6: Variable parameters in five-bar mechanism

Secondly, to reduce viscoelastic deformation, a maximum desired bending angle of 17° was chosen in order to preserve the flexures' shapes.

This section derives of the final gripper dimensions, presents the force versus compression and angular displacement results of the fabricated grippers, and draws a comparison between predicted and experimental results.

A. Gripper Parameter Optimization

A generalized model of the gripper has been derived above, and now the gripper dimensions must be chosen according to the defined constraints. The goal of the optimization is to maximize the change in angle of the gripper fingers, $\Delta\theta_{34}$. Also, since $\Delta\theta_{23}$ is always larger than $\Delta\theta_{34}$, then a design must be chosen which minimizes the difference between these two values. This difference will be referred to as $\Delta\theta_{23-34}$. The reasoning for this is to reduce the maximum stress in structure, which occurs at the flexural hinges and is directly related to the degree of bending.

As illustrated in Figure 6, the three fixed design parameters that affect the bending angles, besides compression, are L_2, L_3 and the difference between L_1 and L_4. A parameter sweep was carried out to observe the trends that arose when varying these values. The dimensions of interest are normalized with respect to the gripper height, L. Therefore, the three ratios of interest are:

$$R_{41} = (L_4 - L_1)/L = L_{41}/L \tag{30}$$

$$R_2 = L_2/L \tag{31}$$

and

$$R_3 = L_3/L \tag{32}$$

1) Observed trends: From an initial parameter sweep, it was concluded that when $R3 > R2$, then $\Delta\theta_{12} > \Delta\theta_{34}$, and vice versa. Only the ranges where R_2 is greater than R_3 were considered for this design since we are interested in larger values of $\Delta\theta_{34}$. The range over which R_2 and R_3 were varied during the parameter sweep were [0.6, 1.0] and [0.2, 0.6], respectively. It was also observed that both negative and positive values of R_{41}, up to a limit of around ± 0.25 (larger values start to result in over-exaggerated, physically infeasible geometries), demonstrated better compression angles than when R_{41} was set to zero. R_{41} was set to -0.2, as negative values of R_{41} produced somewhat larger values of $\Delta\theta_{34}$ and lower $\Delta\theta_{23-34}$ for a given compression than the positive counterpart.

TABLE I: Gripper dimensions

$L(\mu m)$	$L_2(\mu m)$	$L_3(\mu m)$	$L_{41}(\mu m)$	$L_1(\mu m)$	$L_4(\mu m)$
50	40	20	-10	37.5	27.5

Figure 7 shows three pairs of resulting surface plots of $\Delta\theta_{23}$ and $\Delta\theta_{34}$ for gripper compressions of 10%, 15% and 20%. Note that the angles plotted are absolute values measured with respect to the original, uncompressed angles of θ_{23} and θ_{34}; the values for $\Delta\theta_{23}$ are negative, and $\Delta\theta_{34}$ are positive. A number of trends can be inferred from these plots: 1) most intuitively, the absolute values of the angles increase with increasing compression; 2) the lowest combinations of R_3 and R_2 values results in incompatible configurations (i.e. $R_2 + R_3 < 1$) and, therefore, are not plotted; 3) in general, valid combinations of low values of R_2 and R_3 result in higher gripper angles for a given compression, but also the largest values of $\Delta\theta_{23-34}$; 4) for high values of R_3 and low values of R_2, $\Delta\theta_{34}$ starts to become marginally larger than $\Delta\theta_{23}$. This corresponds to the hinges inverting (i.e. the five-bar mechanism becoming a concave pentagon) and is a configuration avoided in these experiments.

The final consideration in choosing R_2 and R_3 was that $\Delta\theta_{23-34}$ should be minimized, as justified previously. Figure 8 plots this value for a compression of 15%. In general, the error decreases as R_2 increases (before inversion), and for R_3 the relationship varies across the range of swept values. Taking into consideration the observed trends in both Figures 7 and 8, a mid-range value of R_3 equal to 0.4 was chosen to increase grasping angle θ_{34} for a given compression; and a mid-range value of R_2 equal to 0.8 was chosen to increase the grasping angle $\Delta\theta_{34}$, to minimize $\Delta\theta_{23-34}$ and to avoid hinge inversion for a reasonable compression. The final gripper dimensions are summarized in Table I.

B. Characterization of Full Gripper

Using the chosen dimensions, the full gripper was fabricated and tested in the same manner as described in Section IV. The gripper design was modified to include a 40 µm tall post which can be easily pressed with the force sensor (which does not fit between the spaces of the fingers).

C. Experimental Versus Theoretical Hinge Rotations - Verification of the Geometric Model

Figure 9 plots the theoretically derived angle values versus the experientially measured ones. The theoretical angles are calculated for same the compression values obtained during the gripper compression test. The experimental results follow closely with the predicted values, although the error appears to increase as the compression increases. This is likely due the fact that flexural hinges do not behave exactly as ideal hinges.

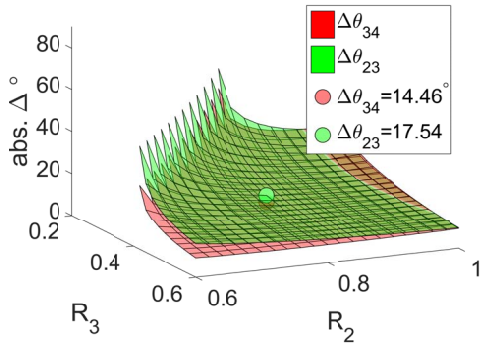

(a) 10% Compression

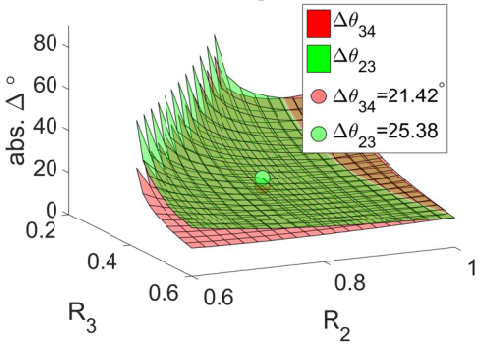

(b) 15% Compression

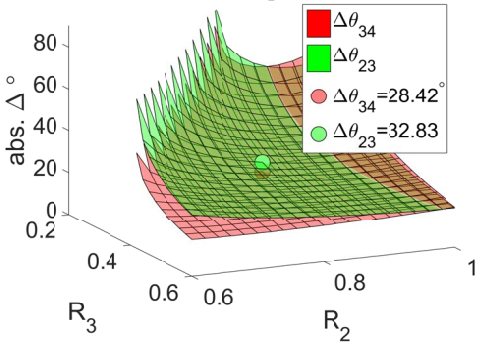

(c) 20% Compression

Fig. 7: Surface plots for $\Delta\theta_{23}$ and $\Delta\theta_{34}$ for varying values of R_2 and R_3, and R_{41} = -0.2 (chosen parameters R_2 = 0.8 and R_3 = 0.4 highlighted)

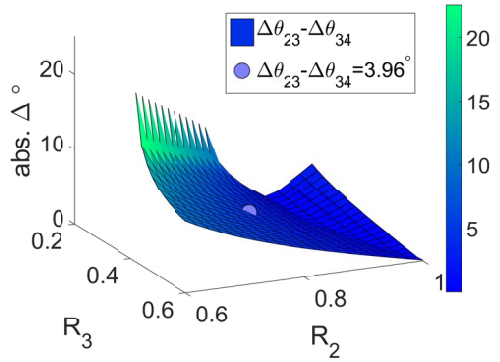

Fig. 8: Absolute difference between $\Delta\theta_{34}$ and $\Delta\theta_{23}$ ($\Delta\theta_{23-24}$) for a compression of 15% (chosen parameters R_2 = 0.8 and R_3 = 0.4 highlighted)

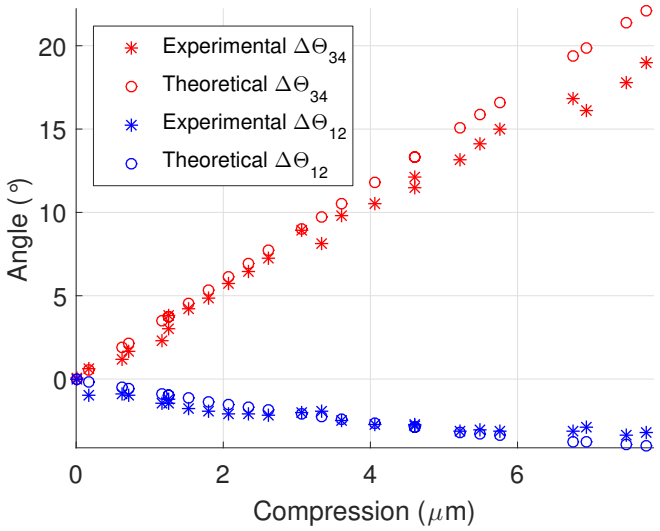

Fig. 9: Experimental vs. theoretical gripper angles

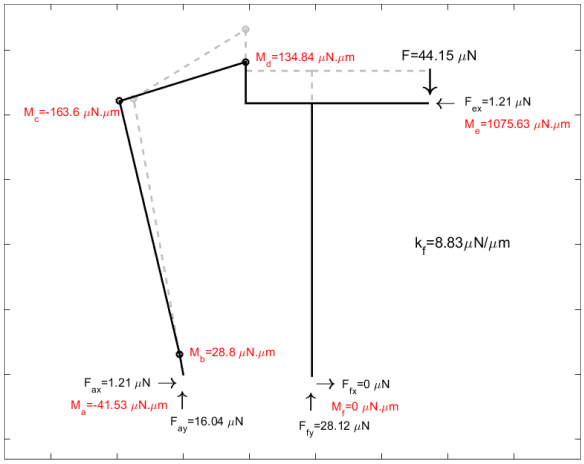

Fig. 10: Static analysis output for compression of 5 μm and resultant finger spring constant, k_f = 8.83 μN/μm

D. Experimental Versus Theoretical Gripper Spring Constant - Verification of the Static Model

The overall gripper spring constant, k_g, is simply calculated using equation 29, as with the linear springs. Calculating the experimental gripper spring constant serves as a direct point of comparison between the experimental data and the previously derived static model from Section III. The three springs plus three five-bar mechanisms with thin flexures effectively act as six parallel springs. Figure 11b summarizes the compression test, which results in an experimental gripper spring constant, $k_{g,ex.}$, of 20.4 μN/μm.

The static model was used to solve for all unknown reaction forces, including the applied compressive force (F), for a given displacement (ΔL). All link lengths are know, and the X- and Y-components (x_n, y_n for n = [1,5]) plus $\Delta\theta$ for each hinge then can be calculated according to Section III.A, as well as the moments of each torsion spring (M_b, M_c and M_d)and the spring reaction force (F_s). From the calculated compressive force and the defined compression,

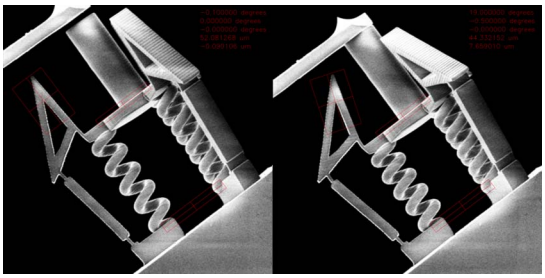

(a) Gripper at 0 µm and 7.5 µm compression

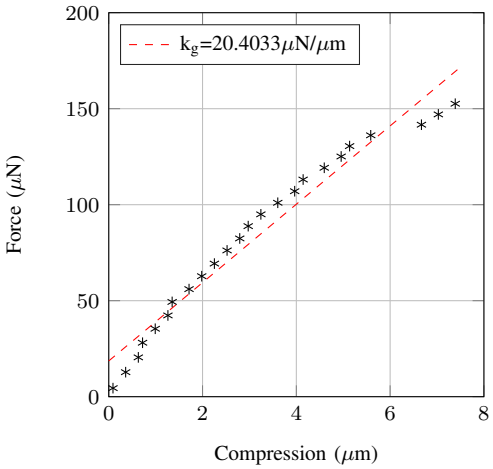

(b) Gripper compression vs. force results

Fig. 11: Full gripper characterization

the overall gripper spring constant is given by:

$$k_g = 3.k_f = 3(F/\Delta L) \tag{33}$$

Figure 10 show the result of solving the static model, after substituting all known and calculated dimensions plus experimentally derived hinge and spring constants. The theoretical finger spring constant (k_f) was calculated to be 8.83 µN/µm, and therefore for the theoretical spring constant for the entire gripper, $k_{g,th.}$, is 3 times this, at 26.49 µN/µm.

The final experimental gripper spring constant, $k_{g,ex.}$ equal to 20.4 µN/µm, is 23% lower that the predicted theoretical spring constant, $k_{g,th.}$ equal to 26.49 µN/µm. The likely reasons behind this discrepancy are discussed next.

E. Sources of Experimental Error

Immediately, it can be observed that the geometric predictions match much more closely to the experimental results that the force-based static analysis prediction. It is logical to conclude that the error is likely to partially arise from incomplete modelling of the viscoelastic material behavior.

Best efforts were made in order to standardize the alignment of the printed grippers during fabrication and characterization, but due to the miniscule size of the gripper, unavoidable alignment errors cannot be completely ruled out. The relative orientations of the force sensor and test structures may vary from experiment to experiment, introducing errors.

Finally, another possible source of error is suspected to be the day-to-day variation within the printing process, as documented by [8]. Variation in the power directly affects the material properties of the bulk material [5], and this effect is particularly apparent if structures not printing on the same 'run'. In the experiments above, the hinges and springs were printed on a separate day to the full gripper model.

VI. Conclusions and Future Work

The design, optimization and testing of the fully 3D, compliant microgripper was presented in this paper. Microfabrication technologies such as TPP help to realize complex 3D tools and offer exciting opportunities to explore new fabrication methods for microrobotics, and this work highlights several potential avenues of research for microsurgical tool development. Overall, despite the discrepancy between the theoretical and experimental gripper spring constant results in the static model, both the geometric and static models still provide a good approximation to help predict and design the tool behavior. Moving forwards, a greater understanding of the material behavior of available commercial photoresists is needed. Alternatively, the development of application-specific, polymerizable materials that demonstrate higher elasticity may help to overcome the undesirable viscoelastic effect. Another avenue for future work is to incorporate a method of active actuation, so that the force actuating the gripper is not provided by the object to be grasped. Actuation mechanisms to be investigated include pneumatic actuation, piezo-electric actuation or stimuli-responsive polymers which could also be printed using TPP.

References

[1] B. J. Nelson, I. K. Kaliakatsos, and J. J. Abbott, "Microrobots for minimally invasive medicine.," *Annual Review of Biomedical Engineering*, vol. 12, pp. 55–85, 2010.

[2] H. Li, G. Go, S. Y. Ko, J.-O. Park, and S. Park, "Magnetic actuated pH-responsive hydrogel-based soft micro-robot for targeted drug delivery," *Smart Materials and Structures*, vol. 25, no. 2, p. 027001, 2016.

[3] E. Gultepe, J. S. Randhawa, S. Kadam, S. Yamanaka, F. M. Selaru, E. J. Shin, A. N. Kalloo, and D. H. Gracias, "Biopsy with thermally-responsive untethered microtools," *Advanced Materials*, vol. 25, pp. 514–519, 2013.

[4] N. Chronis and L. P. Lee, "Electrothermally activated SU-8 microgripper for single cell manipulation in solution," *Journal of Microelectromechanical Systems*, vol. 14, no. 4, pp. 857–863, 2005.

[5] M. Power and G.-Z. Yang, "Optomechanical force estimation using passive micromanipulator end-effectors," in *Int. Conf. on Manipulation, Automation and Robotics at Small Scales*, 2016.

[6] E. Boudreault and C. Gosselin, "Design of Sub-Centimetre Underactuated Compliant Grippers," in *International Design Engineering Technical Conference*, 2006.

[7] T. Frenzel, C. Findeisen, M. Kadic, P. Gumbsch, and M. Wegener, "Tailored Buckling Microlattices as Reusable Light-Weight Shock Absorbers," *Advanced Materials*, pp. 5865–5870, 2016.

[8] M. G. Guney and G. K. Fedder, "Estimation of line dimensions in 3D direct laser writing lithography," *Journal of Micromechanics and Microengineering*, vol. 26, 2016.